

RESEARCH ARTICLE | MARCH 19 2025

Role of interfacial surface anisotropy on liquid grooving at grain boundaries: A phase-field study

Muhammad Umar ; V. Pavan Laxmipathy ; Daniel Schneider ; Michael Selzer ; Britta Nestler 



J. Appl. Phys. 137, 114901 (2025)

<https://doi.org/10.1063/5.0260488>



Articles You May Be Interested In

Investigating the influence of thermal behavior on microstructure during solidification in laser powder bed fusion of AlSi10Mg alloys: A phase-field analysis

J. Laser Appl. (December 2023)

10 April 2025 10:34:40

Instruments for Advanced Science

- Knowledge
- Experience
- Expertise

Click to view our product catalogue

Contact Hiden Analytical for further details:

www.HidenAnalytical.com

info@hiden.co.uk

Gas Analysis

- dynamic measurement of reaction gas streams
- catalysis and thermal analysis
- molecular beam studies
- dissolved species probes
- fermentation, environmental and ecological studies

Surface Science


- UHV TPD
- SIMS
- end point detection in ion beam etch
- elemental imaging - surface mapping

Plasma Diagnostics

- plasma source characterization
- etch and deposition process reaction kinetic studies
- analysis of neutral and radical species

Vacuum Analysis

- partial pressure measurement and control of process gases
- reactive sputter process control
- vacuum diagnostics
- vacuum coating process monitoring



Role of interfacial surface anisotropy on liquid grooving at grain boundaries: A phase-field study

Cite as: J. Appl. Phys. **137**, 114901 (2025); doi: [10.1063/5.0260488](https://doi.org/10.1063/5.0260488)

Submitted: 24 January 2025 · Accepted: 18 February 2025 ·

Published Online: 19 March 2025



Muhammad Umar,^{1,2,a)} V. Pavan Laxmipathy,³ Daniel Schneider,^{1,2,4} Michael Selzer,⁴
and Britta Nestler^{1,2,4}

AFFILIATIONS

¹Institute of Applied Materials—Microstructure Modelling and Simulation, Karlsruhe Institute of Technology (KIT), Strasse am Forum 7, Karlsruhe 76131, Germany

²Institute of Digital Materials Science, Karlsruhe University of Applied Sciences, Moltkestrasse 30, Karlsruhe 76133, Germany

³Max Planck Institute for Dynamics of Complex Technical Systems, Sandtorstrasse 1, Magdeburg 39106, Germany

⁴Institute of Nanotechnology, Karlsruhe Institute of Technology (KIT), Hermann-Von-Helmholtz-Platz 1, Eggenstein-Leopoldshafen 76344, Germany

^{a)}Author to whom correspondence should be addressed: muhammad.umar@partner.kit.edu

ABSTRACT

Engineering materials are polycrystalline in nature, consisting of numerous single crystals interconnected through a three-dimensional interfacial network known as grain boundaries. Often essential in defining the performance and durability of materials, grain boundaries attract considerable attention during alloy development. Initially, we employ a multi-phase-field model and validate the phenomenon of grain-boundary grooving under isotropic energy conditions, with bulk diffusion as the dominant mass transport mechanism. Subsequently, we investigate the effects of interfacial surface anisotropy and crystal misorientation on groove formation. This present study focuses on the effects of interfacial surface anisotropy and crystal misorientation and, thus, allows us to draw comparisons between the effects of different physical phenomena on the grain-boundary behavior. It is observed that the groove kinetics accelerate as a result of fourfold anisotropy, with groove root deepening proportional to the imposed anisotropic strength. Furthermore, the phase-field results presented here align well with theoretical predictions. In addition, we briefly study on the effect of solid–solid anisotropy on the groove root position. We anticipate that the simulated liquid groove and its precise measurement will serve as important tools for studying the relative energies of grain boundaries.

© 2025 Author(s). All article content, except where otherwise noted, is licensed under a Creative Commons Attribution (CC BY) license (<https://creativecommons.org/licenses/by/4.0/>). <https://doi.org/10.1063/5.0260488>

I. INTRODUCTION

Grain-boundary instabilities driven by mass transport mechanisms are crucial for interpreting various processes, such as the sintering of crystalline powders,¹ the motion and coalescence of precipitate particles in alloys,² and the formation of “island” structures in thin films.³ Understanding one such instability, grain-boundary grooving, is often crucial for studying self-similar growth and determining the relative energies of grain boundaries.⁴ In groove dynamics, self-similarity often refers to the evolution of the groove shape over time while preserving its fundamental shape when scaled by its analytically derived power laws. Liquid grooving at grain boundaries occurs whenever a solid–solid phase boundary meets the

surface in a polycrystal. Both from a theoretical and experimental perspective, the seminal concept of grain-boundary grooving was elucidated in detail by Mullins.^{5,6} It was concluded that the groove develops in a self-similar pattern as a result of competing effects of curvature driven gradients and force balance at the triple junction. Depending on the mass transport mechanism, analytical solutions were provided to describe the groove kinetics.

Over the past few years, Mullins’s seminal theory^{5,6} has been extended in several directions^{7–10} to provide a thorough understanding of liquid grooving. For example, Mclean and Hondros⁸ studied experimentally the role of grain-boundary grooving on spheroidization and particle coarsening. It was concluded that the

10 April 2025 10:34:40

equilibrium shape of the grooves was in conjunction with zero creep studies, and the growth rate of the liquid grooves confirmed the presence of volume diffusion as the dominating mass diffusion mechanism. Similarly, Genin *et al.*¹⁰ theoretically studied the effect of stress on grain-boundary grooving under the influence of various transport mechanisms. It was shown that the groove kinetics accelerated as a result of imposed tensile stress.

The development of novel microstructures can be effectively managed through understanding the fundamental forces that lead to pattern formation. Among various physical principles, surface anisotropy of crystal-melt interfacial free energy significantly impacts the dynamics and the behavior of microstructures. Dendrites stand as classical examples that are a result of the force balance between bulk and interfacial contributions of a system.¹¹ In microstructural evolution, interfacial anisotropy, influenced by the orientation of the planar interface relative to the crystal structure, plays a decisive role in pattern selection during solidification. In addition, it is commonly observed that a small change in anisotropy can profoundly alter the dendrite growth velocity and direction. As such, there is a pressing need for precise data on the solid-liquid interfacial anisotropy, especially for metals and alloys that are significant for industrial applications.

We now delve into a range of theoretical, numerical, and experimental studies that examine how surface anisotropy affects the development of grain-boundary grooves in bicontinuous. First, Boiling and Tiller¹² and Nash and Glicksman¹³ provided theoretical perspectives for grain-boundary grooves in the presence of crystal-melt surface tension. In addition, Klinger and Rabkin⁹ modeled faceted grooves and calculated the groove shapes for a wide range of energies and diffusivities. A stability diagram was proposed where it was shown that for large values of grain-boundary energy and high surface energies, the faceted grooves favored for a small inclination of singular surface. Zhang and Gladwell¹⁴ investigated the role of surface anisotropy on grain-boundary grooves driven by surface diffusion. It was showcased that the groove kinetics modified proportionally to the imposed anisotropic strength. For example, in the presence of mild anisotropy, the obtained profiles were self-similar, for critical anisotropy, the grooves were faceted, and for severe anisotropies, the obtained surface was coarsened during the temporal evolution of the grooves. Subsequently, Min and Wong¹⁵ studied the phenomenon of grain-boundary grooving by the inclusion of capillarity-driven surface diffusion with asymmetric and strongly anisotropic surface energies. It was found that the self-similar groove profile was faceted and asymmetric for most bicontinuous. However, for some cases, the development of smooth and symmetric grooves as well as the formation of ridges was noticed.

Over the past two decades, the phase-field approach has become increasingly popular for modeling complex microstructures in solidification,¹⁶ grain-boundary grooves,¹⁷ and flow effects.^{18,19} Several studies have extensively investigated the phenomenon of grain-boundary grooving using the diffuse-interface method.^{17,20–22} For example, Yeh *et al.*²¹ explored the grooving phenomenon for isotropic and anisotropic phase boundaries via focusing on the hump formation on either side of the solid-solid grain boundary. Likewise, Moelans *et al.*²⁰ implemented a phase-field model, which included the orientation of the interfacial energy and thereby

studied the thermal grooving for thin films. Depending upon the mode of diffusion mechanism, the GB grooving was shown in agreement with existing analytical theories. Recently, in our previous work,¹⁷ we explored the presence of an additional convective transport mechanism in the liquid phase and depicted the development of asymmetric groove profiles. After comparing with the sharp-interface theory, it was confirmed that the groove kinetics as well as the grain-boundary grooving mechanism is proportional to the magnitude of convective forces in the bulk liquid phase. Likewise, in a recent investigation, Verma and Mukherjee²² employed a three-dimensional phase-field model and explored the mechanism of corner instability during capillary-driven hole growth in thin films. The effect of various parameters was studied in detail, and it was revealed that the instability observed during hole growth resulted from the saturation of the rim height at the hole's corner, which was linked to the corner's arc length and surface energy anisotropy.

Mukherjee *et al.*^{23,24} employed phase-field simulations to investigate electromigration damage in polycrystalline interconnects, demonstrating how the interplay between surface and grain-boundary diffusion influences the progression of damage through surface drift or intergranular slit formation. Recently, Hoffrogge *et al.*²⁵ extended a grand potential based multiphase-field model to include surface diffusion by elevating diffusion in the interface through a scalar degenerate term, circumventing difficulties in restricting diffusion solely to the interface by combining an Allen-Cahn-type equation with an obstacle-type potential and a conservative diffusion equation.

Most of the aforementioned studies on grain-boundary grooving have primarily focused on the effects of surface diffusion, faceted anisotropy, or convection in the bulk liquid phase. Nonetheless, the existing literature also reveal that a significant gap, i.e., the effect of non-faceted interfacial surface anisotropy during bulk diffusion, remains largely unexplored. The striking morphological and dynamical variations often observed in microstructures suggest that the role and impact of interfacial surface anisotropy are substantial and cannot be neglected. Recognizing this, and based on our earlier work on diffusive-convective transport mechanisms,¹⁷ this work investigates the critical yet unexplored role of interfacial surface anisotropy in grain-boundary grooving and provides a comprehensive study on the role of fourfold interfacial anisotropy. By systematically analyzing the influence of solid-liquid and solid-solid anisotropies, we reveal novel insights into groove root positioning and solutal field modifications. The analytical relationships and theoretical comparisons presented here not only extend our understanding of grain-boundary phenomena but also offer a more nuanced perspective on how interfacial energy variations can significantly impact microstructural evolution in polycrystalline materials.

This paper is organized as follows: after the introduction, we provide the phase-field model with the governing equations, where the anisotropy function as well as all parameters required to simulate the current set of simulations are provided. Next, we present the phenomenon of grain-boundary grooving as a result under isotropic energy conditions, with bulk diffusion as the dominant mass transport mechanism, and we compare the two-dimensional phase-field results with the seminal work of Mullins.⁶ Afterward, we carry out and study the role of solid-liquid interfacial anisotropy on groove kinetics. Additionally, we perform

a direct comparison with grooves developed with inter-phase boundary anisotropy. Finally, we conclude our manuscript with a brief summary and outlook.

II. PHASE-FIELD MODEL

The phase-field approach has emerged as a preferred method for modeling intricate microstructures and has steadily gained recognition for its computational effectiveness and versatility in capturing the underlying physics. In the present work, the phase-field model employed is based on the grand potential formulation by Choudhury and Nestler.^{16,17,26} This formulation begins with the grand potential functional, which is given as

$$\Omega(T, \mu, \boldsymbol{\phi}) = \int_{\Omega} \left[\Psi(T, \mu, \boldsymbol{\phi}) + \left(\varepsilon a(\boldsymbol{\phi}, \nabla \boldsymbol{\phi}) + \frac{1}{\varepsilon} \omega(\boldsymbol{\phi}) \right) \right] d\Omega, \quad (1)$$

where T is the temperature in the domain, ε is an interface width parameter, μ represents the chemical potential, and $a(\boldsymbol{\phi}, \nabla \boldsymbol{\phi})$ and $\omega(\boldsymbol{\phi})$ represent the gradient energy density contribution and double obstacle potential density at the interface between two phases, respectively. $\boldsymbol{\phi} = \{\phi_\alpha, \phi_\beta, \dots, \phi_N\}$ is order parameter vector containing individual order parameters for $N = 3$ phases in the domain that represents solid 1, solid 2, and liquid. The grand chemical potential $\Psi(T, \mu, \boldsymbol{\phi})$ is a vector containing the individual grand potentials $\Psi_\alpha(T, \mu)$ of all phases interpolated with a function $h_\alpha(\boldsymbol{\phi}) = \phi_\alpha^2(3 - 2\phi_\alpha)$ as

$$\Psi(T, \mu, \boldsymbol{\phi}) = \sum_{\alpha=1}^N \Psi_\alpha(T, \mu) h_\alpha(\boldsymbol{\phi}), \quad (2)$$

$$\Psi_\alpha(T, \mu) = f_\alpha(c^\alpha(\mu, T)) - \mu \cdot c^\alpha(\mu, T). \quad (3)$$

The term $f_\alpha(c^\alpha(\mu, T))$ is the bulk Gibbs energy of phase α , which is taken as a simplified parabolic function for all the phases (see Refs. 18 and 27 for more details). $c^\alpha(\mu)$ represents the composition of solute in phase α .

The evolution equation for ϕ_α is derived from the grand potential functional using the variational calculus approach, which is given as

$$\tau \varepsilon \frac{\partial \phi_\alpha}{\partial t} = \varepsilon \left(\nabla \cdot \frac{\partial a(\boldsymbol{\phi}, \nabla \boldsymbol{\phi})}{\partial \nabla \phi_\alpha} - \frac{\partial a(\boldsymbol{\phi}, \nabla \boldsymbol{\phi})}{\partial \phi_\alpha} \right) - \frac{1}{\varepsilon} \frac{\partial \omega(\boldsymbol{\phi})}{\partial \phi_\alpha} - \frac{\partial \Psi(T, \mu, \boldsymbol{\phi})}{\partial \phi_\alpha} - \lambda, \quad (4)$$

where τ is a relaxation coefficient at the interface taken as a constant value given in Table I and λ is a Lagrange multiplier incorporated such that the local constraint $\sum_{\alpha=1}^N \phi_\alpha = 1$ is fulfilled. The expression for λ reads as

$$\lambda = -\frac{1}{N} \sum_{\beta=1}^N \varepsilon \left(\nabla \cdot \frac{\partial a(\boldsymbol{\phi}, \nabla \boldsymbol{\phi})}{\partial \nabla \phi_\beta} - \frac{\partial a(\boldsymbol{\phi}, \nabla \boldsymbol{\phi})}{\partial \phi_\beta} \right) - \frac{1}{\varepsilon} \frac{\partial \omega(\boldsymbol{\phi})}{\partial \phi_\beta} - \frac{\partial \Psi(T, \mu, \boldsymbol{\phi})}{\partial \phi_\beta}, \quad (5)$$

TABLE I. Simulation parameters for the present study.

Description	Value
Partition coefficient (k)	0.25
Diffusion coefficient (D^β)	$2 \times 10^{-9} \text{ m}^2/\text{s}$
Discretized grid space ($\Delta x = \Delta y$)	$0.5 \times 10^{-7} \text{ m}$
Interface width parameter (ε)	$2.0 \times 10^{-7} \text{ m}$
Relaxation coefficient (τ)	$6 \times 10^6 \text{ J/s m}^4$
Surface energy ($\gamma_{\alpha\beta}$)	0.5 J/m^2

where ϕ_β denotes a phase in the domain other than ϕ_α which already appeared in Eq. (4). In general, all bold quantities represent vectors, i.e., $\boldsymbol{\phi}$ is a vector corresponding to non-conserved phase-field order parameter containing the volume fractions of $N = 3$ phases in the system.

$\omega(\boldsymbol{\phi})$ is the double obstacle potential density, which is given as

$$\omega(\boldsymbol{\phi}) = \frac{16}{\varepsilon \pi^2} \sum_{\alpha, \beta=1}^{N,N} \gamma_{\alpha\beta} \phi_\alpha \phi_\beta + \frac{1}{\varepsilon} \sum_{\alpha, \beta=1}^{N,N,N} \gamma_{\alpha\beta\delta} \phi_\alpha \phi_\beta \phi_\delta, \quad (6)$$

The gradient energy term reads as

$$a(\boldsymbol{\phi}, \nabla \boldsymbol{\phi}) = \sum_{\alpha, \beta=1}^{N,N} \gamma_{\alpha\beta} [a_c(\mathbf{q}_{\alpha\beta})]^2 |\mathbf{q}_{\alpha\beta}|^2, \quad (7)$$

where $\gamma_{\alpha\beta}$ is the interfacial energy per unit area at the α/β interface. For isotropic interfaces, our previous studies^{28,29} have explored the evolution of isotropic microstructures by using the condition ($a_c(\mathbf{q}_{\alpha\beta}) = 1$). For interfaces with finite interfacial anisotropy, an underlying fourfold cubic symmetry is modeled by the expression

$$a_c(\mathbf{q}_{\alpha\beta}) = 1 - \delta_{\alpha\beta} \left(3 - 4 \frac{|\mathbf{q}_{\alpha\beta}|_4^4}{|\mathbf{q}_{\alpha\beta}|^4} \right), \quad (8)$$

where $|\mathbf{q}_{\alpha\beta}|_4^4 = \sum_{i=1}^d (\mathbf{q}_{\alpha\beta,i}^4)$, $|\mathbf{q}_{\alpha\beta}|^4 = [\sum_{i=1}^d (\mathbf{q}_{\alpha\beta,i}^2)]^2$, and i denotes the number of dimensions for which the formulation is used in a simulation study. $\mathbf{q}_{\alpha\beta} = \phi_\beta \nabla \phi_\alpha - \phi_\alpha \nabla \phi_\beta$ is the generalized gradient normal vector. In the present model, since we can independently set the anisotropic properties for each interface, the strength of the anisotropy of the respective α/β interface is given by the parameter $\delta_{\alpha\beta}$. The anisotropic formulation $a_c(\mathbf{q}_{\alpha\beta})$ is also the function of the local misorientation of bicrystal rotated with respect to its reference configuration given by an angle $\theta_{\alpha\beta}$, which can be correlated with the anisotropy function $a_c(\mathbf{q}_{\alpha\beta})$. To show this relationship, we first write the anisotropy function for 2D with components of $\mathbf{q}_{\alpha\beta}$,

$$a_c(\mathbf{q}_{\alpha\beta}) = 1 - \delta_{\alpha\beta} \left(3 - 4 \frac{\mathbf{q}_{\alpha\beta,x}^4 + \mathbf{q}_{\alpha\beta,y}^4}{\mathbf{q}_{\alpha\beta,x}^4 + \mathbf{q}_{\alpha\beta,y}^4 + 2\mathbf{q}_{\alpha\beta,x}^2 \mathbf{q}_{\alpha\beta,y}^2} \right), \quad (9)$$

where $\mathbf{q}_{\alpha\beta,x}$ and $\mathbf{q}_{\alpha\beta,y}$ are x and y components of the gradient vector $\mathbf{q}_{\alpha\beta}$, respectively. $\mathbf{q}_{\alpha\beta}$ can be written in the vector form as

$$\mathbf{q}_{\alpha\beta} = \begin{bmatrix} \mathbf{q}_{\alpha\beta,x} \\ \mathbf{q}_{\alpha\beta,y} \end{bmatrix}.$$

To consider the role of misorientation angle $\theta_{\alpha\beta}$, we implement a rotation matrix $R_{\alpha\beta}$ for the interface between α and β ,

$$R_{\alpha\beta}(\theta_{\alpha\beta}) = \begin{bmatrix} \cos(\theta_{\alpha\beta}) & -\sin(\theta_{\alpha\beta}) \\ \sin(\theta_{\alpha\beta}) & \cos(\theta_{\alpha\beta}) \end{bmatrix}.$$

To obtain the rotated normal vector $\mathbf{q}_{\alpha\beta,rot}$, matrix multiplication of transpose of rotation matrix with gradient normal vector, i.e., $\mathbf{q}_{\alpha\beta}^{rot} = R_{\alpha\beta}^T \cdot \mathbf{q}_{\alpha\beta}$ is performed and the x, y components of the $\mathbf{q}_{\alpha\beta}$ in Eq. (9) are replaced with the rotated ones to modify the gradient energy density as $a_c(\mathbf{q}_{\alpha\beta}^{rot}(\theta_{\alpha\beta}))$. In addition, the dot product of the transpose of $R_{\alpha\beta}$ with the $\mathbf{q}_{\alpha\beta}$ yields the resulting gradient energy density rotated in the counterclockwise direction.

Moreover, since heat and mass transport occur at significantly different time scales during phase transformation, for the present study, the conduction of heat is treated as isothermal and the temperature T in Eq. (4) is assumed constant throughout the system and henceforth plays no role in our study. Now, the evolution equation for the chemical potentials can be expressed as

$$\frac{\partial \mu}{\partial t} = \left[\sum_{\alpha=1}^N h_{\alpha}(\boldsymbol{\phi}) \frac{\partial c^{\alpha}(\mu)}{\partial \mu} \right]^{-1} \left\{ \nabla \cdot (\mathbf{M}(\boldsymbol{\phi}) \nabla \mu - \mathbf{J}_{at}) - c^{\alpha}(\mu) \frac{\partial h_{\alpha}(\boldsymbol{\phi})}{\partial t} \right\}. \quad (10)$$

where $\mathbf{M}(\boldsymbol{\phi}) = \sum_{\alpha=1}^N D_{\alpha} \frac{\partial c}{\partial \mu} g_{\alpha}(\boldsymbol{\phi})$ is the interface mobility, D_{α} is the diffusivity matrix, and $g_{\alpha}(\boldsymbol{\phi})$ is a higher order polynomial such that it interpolates the mobilities across the solid-liquid interface. In addition, $c^{\alpha}(\mu)$ is the chemical potential dependent chemical composition in phase α . In Eq. (10), the flux on the right-hand side has contributions from diffusion due to the gradient in chemical potentials and interface mobility. The anti-trapping current \mathbf{J}_{at} on the right-hand side addresses the solute trapping effect due to an enlarged diffuse-interface width in our model, which reads as

$$\mathbf{J}_{at} = -\frac{\pi \varepsilon g_{\alpha}(\boldsymbol{\phi}) [1 - h_{\alpha}(\boldsymbol{\phi})]}{4 \sqrt{\phi_{\alpha}(1 - \phi_{\alpha})}} [c^{\beta}(\mu, T) - c^{\alpha}(\mu, T)] \frac{\partial \phi_{\alpha}}{\partial t} \frac{\nabla \phi_{\alpha}}{|\nabla \phi_{\alpha}|}. \quad (11)$$

For the present study, the numerical parameters are provided in Table I, while the model related information is discussed in detail by Choudhury and Nestler.^{26,30} Last, while Eqs. (4) and (10) are numerically solved in space via a finite difference discretization, the time derivative follows an explicit Euler scheme. Finally, the current numerical algorithm is parallelized via message passing interface (MPI) to distribute the computing task on multicore high performance architectures.

III. RESULTS AND DISCUSSION

A. Isotropic liquid groove

In this section, we examine the role of bulk diffusion, where diffusion occurs through the movement of atoms at their respective lattice sites at the atomic level, often driven by concentration gradients in the liquid phase. We first benchmark our initial conditions considering a numerical domain of 750×200 cells and $\Delta x = \Delta y = 0.5 \times 10^{-7}$ m, with the ratio $\frac{\Delta x}{\varepsilon} = 0.25$ [see Fig. 1(a)].

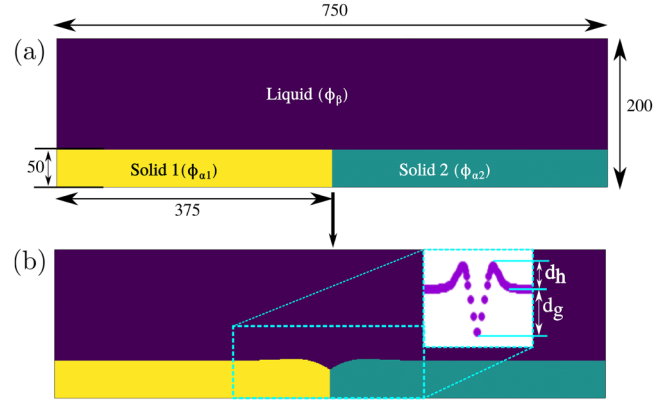


FIG. 1. (a) and (b) Two-dimensional phase-field simulation of grain-boundary grooving in a semi-infinite bicrystal system containing three phases, i.e., liquid, solid 1, and solid 2. Initialized with a dihedral angle Φ of 180° , the groove develops as a result of force balance at the triple junction.

In total, the three non-conserved order parameters, i.e., $\phi_{\alpha1}$, $\phi_{\alpha2}$, and ϕ_{β} correspond to the three phases, i.e., solid 1, solid 2, and liquid, respectively, as shown in Fig. 1(a). Here, Δx is the discretized unit cell along the x -direction and ε is the width of the diffuse interface. The independence of the initial solid and liquid thicknesses in the simulation domain is verified prior to the simulation study, as detailed in Appendix A. Furthermore, Neumann boundary conditions are applied on the lateral sides via setting the directional derivatives normal to the domain boundaries to zero. Figures 1(a) and 1(b) depict the temporal evolution of the grain-boundary groove, where the symmetric groove evolves as a result of force balance and curvature dependent chemical potentials near the solid-liquid interface. Initialized with a dihedral angle of 180° at the triple junction, the solute atoms tend to leave the curved surface and consequently force the groove to deepen with time. As the mass transport near the solid-liquid interface is driven by bulk diffusion, we notice the symmetric nature of the V-shaped groove through the $\phi = 0.5$ iso-lines in Fig. 2. We now calculate the groove depth ($d_g + d_h$) from the ridge height for each timestep, and Fig. 3 demonstrates its relation with simulation time. The analytical fit $(d_g + d_h) \propto t^n$ gives us an exponent $n = 0.334$, an excellent agreement with Mullins's theory for bulk diffusion.⁶ Details on the calculation of the doubling of the groove depth ($d_g + d_h$) when the time is increased by a factor of eight are provided in Appendix B. In essence, this quantitative agreement illustrates that the groove profile doubles its size, i.e., groove depth ($d_g + d_h$) whenever we increase the time by a factor of eight.

To further validate our two-dimensional simulation, we investigate the role of surface energies. We systematically decrease the ratio R_0 , where R_0 is the ratio between the grain-boundary energy $\gamma_{\alpha1\alpha2}$ to the solid-liquid interfacial energy $\gamma_{\alpha\beta}$. For a solid-solid grain boundary, which is normal to the free surface, we consider the relation between the equilibrium dihedral angle Φ at the triple junction, and the surface energies, given by $R_0 = \frac{\gamma_{\alpha1\alpha2}}{\gamma_{\alpha\beta}} = 2 \cos(\frac{\Phi}{2})$, where $\gamma_{\alpha1\alpha2}$ is referred as grain-boundary energy, and $\gamma_{\alpha\beta}$ is the

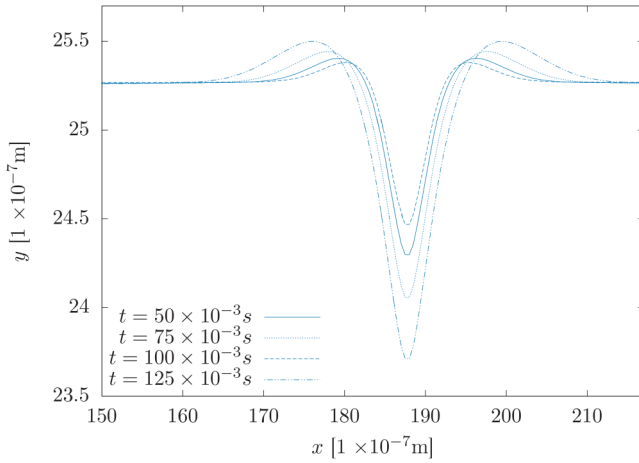


FIG. 2. Isolines depicting the temporal evolution of isotropic grain-boundary grooves. Symmetric groove profiles develop as a result of bulk diffusion in the liquid phase. Various dashed lines represent phase-field isolines from different timesteps.

interfacial energy of the solid-liquid interface. Furthermore, the slope m at the root position with respect of the initial flat interface is given as $m = \cot(\frac{\Phi}{2})$. Combining the two,

$$m = \cot\left(\frac{\Phi}{2}\right) \quad (12)$$

and

$$m = \frac{\cos(\frac{\Phi}{2})}{\sqrt{1 - \cos^2(\frac{\Phi}{2})}}, \quad (13)$$

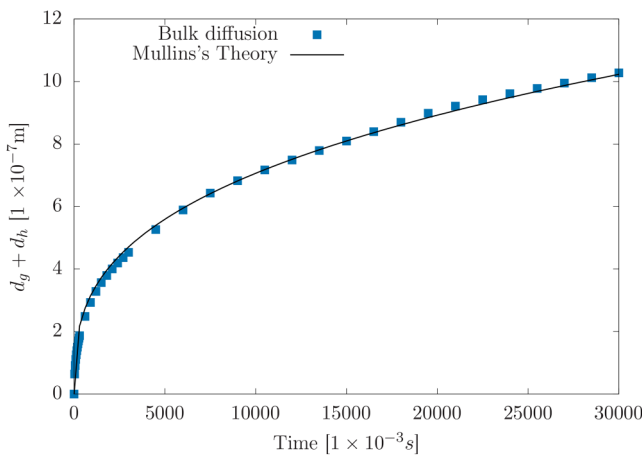


FIG. 3. Groove depth ($d_g + d_h$) as a function of simulation time. A non-linear analytical fit in excellent agreement with Mullins's power law.

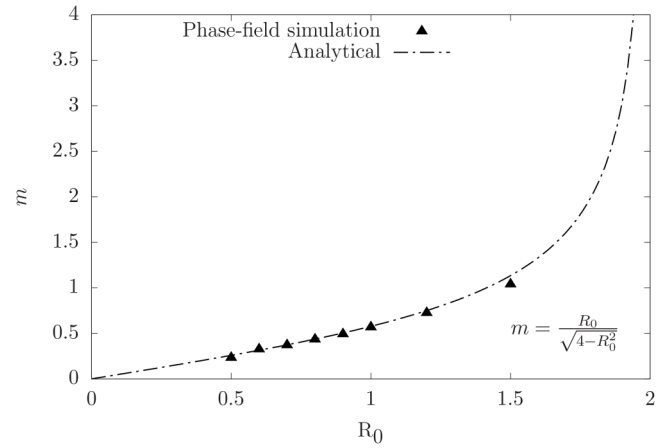


FIG. 4. Groove root slope m as a function of R_0 , where R_0 is the ratio between the solid-solid interfacial energy ($\gamma_{\alpha_1\alpha_2}$) to the solid-liquid interfacial energy ($\gamma_{\alpha\beta}$). Obtained slopes from various simulations agree well with Eq. (14).

we get

$$m = \frac{R_0}{\sqrt{4 - R_0^2}}. \quad (14)$$

Here, $R_0 = \frac{\gamma_{\alpha_1\alpha_2}}{\gamma_{\alpha\beta}}$. The above relation is validated in Fig. 4, where an excellent agreement with the calculated groove root slopes for various two-dimensional simulations is observed. As the ratio $\frac{\gamma_{\alpha_1\alpha_2}}{\gamma_{\alpha\beta}}$ varies from 0 to 2, we discern that the slope m varies from 0 to infinity (see Fig. 4). With $R_0 = 1$ for the present study, the calculated slope $m = 0.556$ correspondingly agrees well with the typical values recorded in experimental studies.³¹ Finally, we have confirmed that the selected numerical parameters are well within the limit and the phase-field results become virtually independent of the diffuse-interface width. With our parameters benchmarked for the bulk diffusion, we now proceed to examine the role of interfacial surface anisotropy on liquid grooving in Secs. III B–III D.

B. Role of solid-liquid interfacial anisotropy

It is well known that the imposed solid-liquid interfacial anisotropy plays a pivotal role in crystal shape evolution. For example, depending upon the type of anisotropy, i.e., fourfold or sixfold, and the anisotropic strength, the interface evolves in a pattern-like structure along a specific direction.

In this section, we exemplarily illustrate the role of fourfold interfacial anisotropy on the kinetics of liquid grooving. Herein, we limit ourselves to anisotropy strengths such that the interface stiffness remains positive and the anisotropic strength is less than $1/15$.³² Moreover, we know that the surface stiffness³³ is defined as, $a_c(\mathbf{q}_{\alpha\beta}(\theta_{\alpha\beta})) + a_c''(\mathbf{q}_{\alpha\beta}(\theta_{\alpha\beta})) \geq 0$, where $a_c(\mathbf{q}_{\alpha\beta}(\theta_{\alpha\beta}))$ is misorientation dependent gradient energy. The interface stiffness at any misorientation angle $\theta_{\alpha\beta}$ must yield the anisotropic strength $\delta_{\alpha\beta}$ to be non-negative and less than $1/15$ for the interface to be stable.

10 April 2025 10:34:40

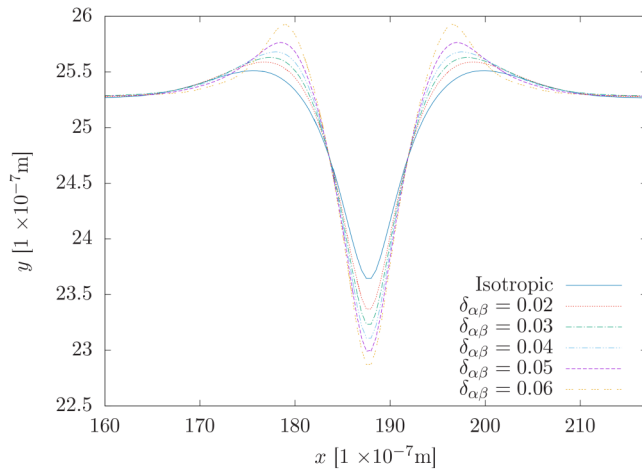


FIG. 5. Groove profiles at various anisotropic strengths $\delta_{\alpha\beta}$. An increase in the anisotropic strength proportionately deepens the groove root position.

The parameter $\delta_{\alpha\beta}$ influences the morphology and growth patterns of solidifying interfaces. Figure 5 describes the evolution of the groove profiles at various $\delta_{\alpha\beta}$, where we observe that apart from the groove ridge positions, there is no significant morphological difference in the morphologies when compared with the isotropic groove, as illustrated in the earlier section. However, a closer look depicts that the width of the groove pit region decreases with the decrease in the anisotropic strength. This morphological feature is depicted through the pit region in Fig. 6, where the isolines appear to be widening at weaker anisotropies.

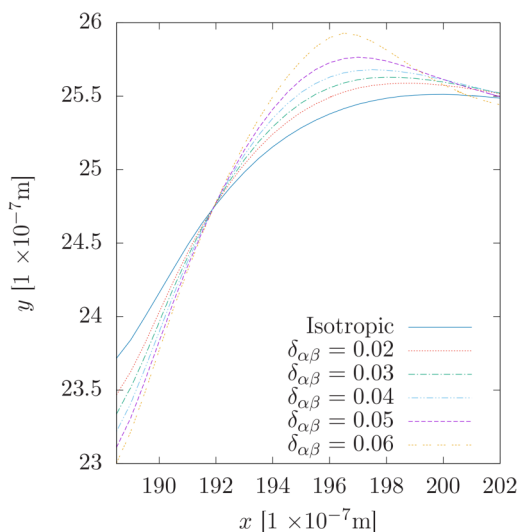


FIG. 6. Groove pit region at various anisotropic strengths. The width of the pit region narrows as the anisotropic strength is increased.

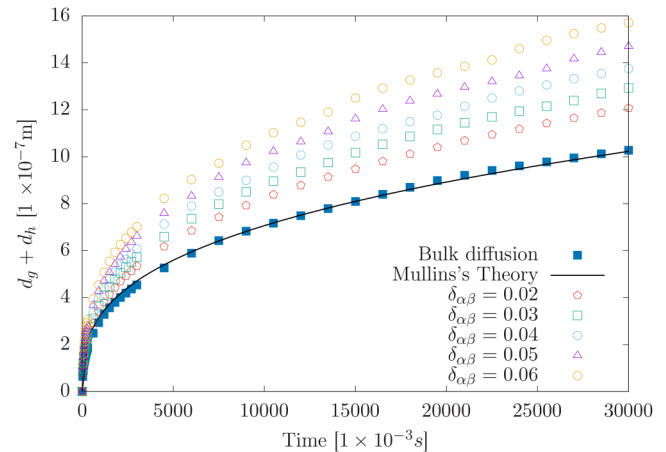


FIG. 7. Groove depth from the ridge height ($d_g + d_h$) as a function of simulation time. With an increase in the anisotropic strength, the groove root deepens at a faster rate, deviating significantly from Mullins's theory (solid line) for an isotropic grain-boundary groove. For isotropic grain boundaries, excellent agreement with Mullins's theory is observed (black squares).

In general, the curvature of the groove profile varies from point to point and causes a difference in chemical potential of atoms along the solid-liquid interface. These curvature driven gradients developed near the pit region in turn govern the groove kinetics. On the other hand, at higher $\delta_{\alpha\beta}$, the contribution from the anisotropy in the interfacial energy dominates, and, therefore, the root position responds to the modification of solutal fields and evolves toward the steepest chemical gradient in the liquid phase. The solid-liquid interfacial energy and the chemical potentials in the groove pit region dynamically compete with each other and determine the groove kinetics at the grain boundary.

This behavior is similar to an experimental observation from Gladwell and co-workers,³⁴ albeit for surface diffusion, where the groove morphology remained unchanged for various anisotropic strengths $\delta_{\alpha\beta} < 0.06$. In addition, other numerical studies^{35,36} have also observed minimal variation in profile shapes, especially for weak anisotropies. However, in contrast to a previous study,³⁷ we have implemented non-faceted interfacial anisotropy, and as a result the non-faceted growth of the diffuse interface is preserved during the temporal evolution of liquid grooves.

We now calculate the groove depth for each case and compare directly with the isotropic groove kinetics. From Fig. 7, we notice that the evolution of the groove depth, and consequently, the power law differs significantly with the increase in the anisotropic strength $\delta_{\alpha\beta}$. Likewise, from a non-linear analytical fit in Fig. 7, we find a significant deviation of the exponent $n > 0.33$ from Mullins's classical law.

C. Role of crystal misorientation

In Sec. III B, we have observed that the interfacial anisotropy plays a crucial role at the triple junctions and accordingly acts as an important parameter to determine the self-similar growth of liquid grooves.

In general, self-similarity of liquid grooves refers to the preservation of geometric or kinematic properties across different time and length scales. Persisting across varying diffusion mechanisms, such a time-independent behavior provides us with insight into the fundamental physics of liquid grooving and allows for more generalized predictions of groove behavior. In addition, modifying the misorientation angle $\theta_{\alpha\beta}$ between the crystalline axis and the growth direction y in turn modifies the anisotropy function operating in the growth plane. The crystallographic misorientation of the growing phase is taken into account with the help of the normal vector to the interface. Finally, the gradient energy density $a_c(\mathbf{q}_{\alpha\beta}(\theta_{\alpha\beta}))$ accounts for the local misorientation of the growing phase. For example, competition between different orientations has been studied to shed some light on the development of a preferred crystallographic direction during dendritic solidification.^{16,38}

In Fig. 8, we demonstrate the groove profiles for $\delta_{\alpha\beta} = 0.04$, where we notice that the groove pit morphology as well as the groove root position is modified as a result of the imposed misorientation angle. Here, the reference configuration $\theta_{\alpha\beta} = 0$ indicates that the orientation of minimal interfacial energy is aligned with the growth direction. During liquid grooving, the system evolves in order to reduce its overall free energy; however, if the interfacial energy varies with local orientation, which is characteristic of crystalline materials, preference is given to surfaces of low energy with the resulting equilibrium shape being non-spherical or polyhedral. As a result, the groove morphology changes as we change the misorientation angle, as shown in Fig. 8.

Voorhees *et al.*³⁹ studied the role of interfacial surface anisotropy and calculated the relation between surface tension anisotropy and the depth of the groove. Using $\gamma_{\alpha\beta} = 1 + \delta_{\alpha\beta}\cos(4\theta + \theta_{\alpha\beta})$ for a fourfold anisotropy, the groove depth was calculated as

$$d_g = 2[1 + \delta_{\alpha\beta}(-4\sin 4\theta_{\alpha\beta} + \cos 4\theta_{\alpha\beta})]^{1/2}. \quad (15)$$

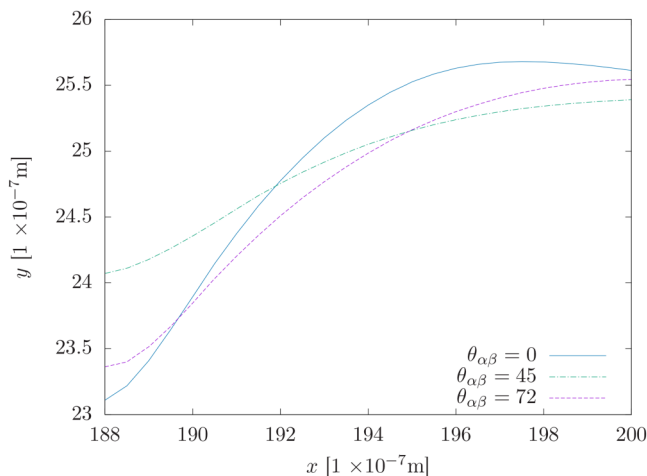


FIG. 8. Groove isolines for different orientation angles. The groove pit region changes as a result of the orientation of the crystal to the growth direction.

Here, $\delta_{\alpha\beta}$ is the strength of the anisotropy and $\theta_{\alpha\beta}$ is the misorientation angle. As shown in the relationship as well in our numerical results, $\theta_{\alpha\beta}$ clearly modifies the position of the groove root and thus the magnitude of the groove depth as a result of modifying the position of extremas in the surface stiffness relative to the growth direction. By and large, the significant differences in these groove profiles in Fig. 8 emphasize the necessity of considering the crystal orientation relative to the growth direction, as well as the magnitude of the interfacial surface anisotropy. Such a combined understanding is, therefore, crucial in order to fully comprehend the resulting grain-boundary groove morphology.

D. Role of solid-solid anisotropy

As a common material application, eutectic solidification microstructures are a classic example where grain-boundary grooving is of great relevance. In general, regular eutectics feature solid-liquid interfaces that are atomically rough and exhibit minimal anisotropy. In contrast, solid-solid interfaces are typically highly anisotropic, often resulting in distinctive morphological features in three phase systems.⁴⁰ In this regard, we qualitatively illustrate and compare the groove profiles for solid-solid and solid-liquid anisotropy. For the sake of clarity, we emphasize that, in Secs. III A–III C, the solid-solid interface anisotropy was zero, i.e., $\delta_{\alpha_1\alpha_2} = 0$. Herein, we impose the solid-solid anisotropy with $\delta_{\alpha_1\alpha_2} = 0.04$, where $\alpha_1\alpha_2$ represents the interface boundary between the two solid phases. In Fig. 9, we observe that when compared with the anisotropy in the solid-liquid interface $\delta_{\alpha\beta} = 0.04$, the grooves with inter-phase boundary are shallower. The grain-boundary groove developed as a result of solid-solid anisotropy restricts the formation of deeper groove pits as a result of increased surface stiffness along the solid-solid grain boundary. Likewise, grooves influenced by solid-liquid anisotropy exhibit higher ridge heights on either side of the pit region. Nevertheless, upon closer examination, it is also evident that the groove width is greater in the case of solid-solid anisotropy.

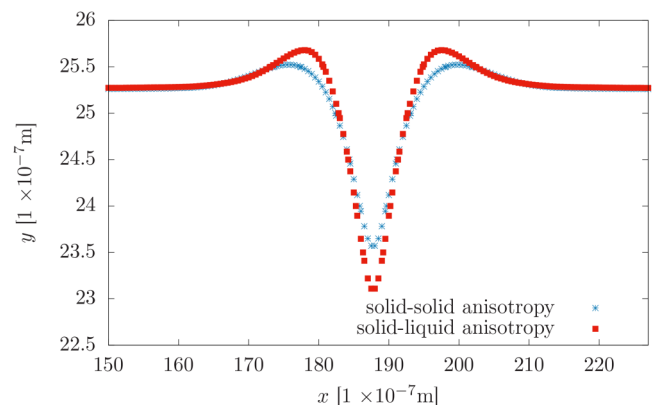


FIG. 9. Grain-boundary groove profiles with solid-solid and solid-liquid anisotropy. The presence of solid-solid anisotropy restricts groove root deepening.

10 April 2025 10:34:40

IV. SUMMARY AND OUTLOOK

In conclusion, we utilized a multi-phase-field method to explore the influence of interfacial surface anisotropy on grain-boundary grooving. Initially, we validated the phenomenon of grain-boundary grooving by considering bulk diffusion in the liquid phase as the mass transport mechanism. Following this, we examined the effect of fourfold interfacial surface anisotropy on the groove kinetics. Our observations revealed that the solid-liquid anisotropy accelerates groove dynamics as a result of altering the solutal fields near the groove pit region. We have also provided a direct comparison with theoretical predictions, highlighting the influence of misorientation angle on the groove root position, and presented an analytical relationship. Additionally, we investigated the role of solid-solid anisotropy on the groove root position and noticed that the root position is shallower in contrast to the groove root for solid-liquid anisotropy.

As a topic of future interest, we plan to study the combined effects of stress in the presence of different transport mechanisms, such as surface diffusion and bulk diffusion. Further possible extension toward three-dimensional thin films is planned to provide a comprehensive understanding of grain-boundary grooving in polycrystalline thin films. Last, a study on the interplay between corrosion and grain-boundary grooving, particularly under the influence of grain-boundary diffusion, promises to uncover vital insights into material degradation processes.

ACKNOWLEDGMENTS

M.U. gratefully acknowledges financial support of the German Research Foundation (DFG) in the framework of Project No. 434946896 within the research unit FOR5134 (TP6), “Erstarrungsrisse beim Laserstrahlschweißen: Hochleistungsrechnen für Hochleistungsprozesse—Mikrostruktursimulation der Erstarrung in der Schweißnaht.” M.S. and B.N. acknowledge financial support by the Helmholtz Association through the programme “MSE,” No. 43.31.01. This work was performed on the bwUniCluster computing resource, which is funded by the Ministry of Science, Research and the Arts of Baden-Württemberg and the Universities of Baden-Württemberg, as part of the bwHPC programme. Fruitful discussions and previous work of Paul Wilhelm Hoffrogge and Nick Streichhan are thankfully acknowledged.

AUTHOR DECLARATIONS

Conflict of Interest

The authors have no conflicts to disclose.

Author Contributions

M. Umar and V. P. Laxmipathy contributed equally to this work.

Muhammad Umar: Conceptualization (equal); Formal analysis (equal); Investigation (equal); Methodology (equal); Software (equal); Visualization (equal); Writing – original draft (equal).
V. Pavan Laxmipathy: Conceptualization (equal); Formal analysis (equal); Investigation (equal); Methodology (equal); Software (equal); Visualization (equal); Writing – original draft (equal).

Daniel Schneider: Project administration (equal); Resources (equal); Supervision (equal); Writing – review & editing (equal).
Michael Selzer: Project administration (equal); Resources (equal); Software (lead); Supervision (supporting); Validation (supporting); Visualization (equal); Writing – review & editing (supporting).
Britta Nestler: Funding acquisition (lead); Investigation (equal); Project administration (equal); Resources (equal); Software (supporting); Supervision (lead); Validation (lead); Writing – review & editing (equal).

DATA AVAILABILITY

The data that support the findings of this study are available from the corresponding author upon reasonable request.

APPENDIX A: INFLUENCE OF INITIAL SOLID AND LIQUID THICKNESSES IN SIMULATION DOMAIN

The influence of initial solid thickness on the liquid groove profile was investigated in this section. Herein, we perform four different simulations with varying initial solid phase thicknesses (50, 75, 100, and 125 numerical cells), as illustrated in Figs. 10(a)–10(d).

To quantitatively validate the evolution of the groove across different cases, we calculate the groove depth ($d_g + d_h$) as a function of simulation time. The results demonstrate that the groove profile evolves identically across all examined cases, indicating that

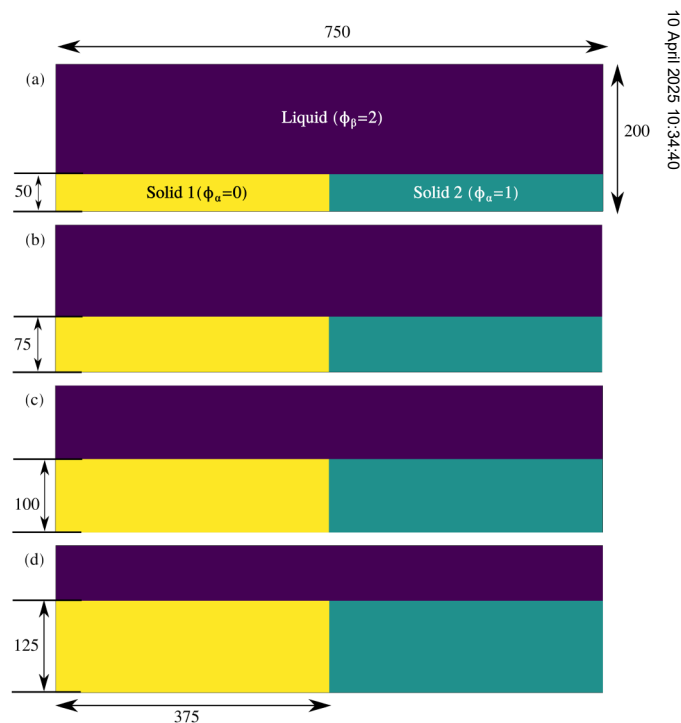


FIG. 10. (a)–(d) Two-dimensional domain with changing initially considered solid phase thickness from 50 to 125.

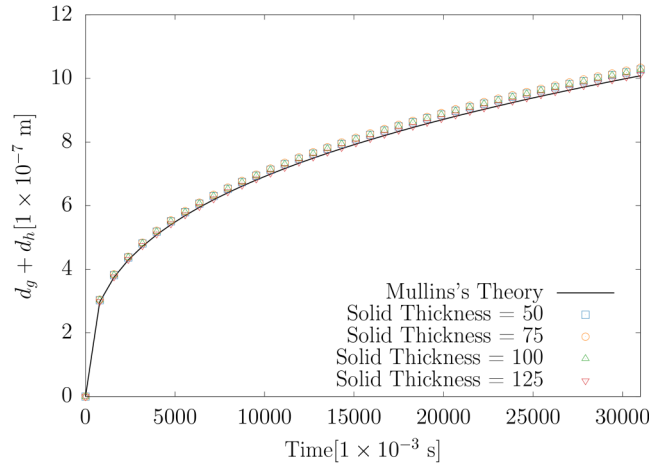


FIG. 11. Groove depth plotted as a function of simulation time for various solid phase thicknesses. All the cases showcase an excellent agreement with Mullins's study.

the groove dynamics is independent of the initial solid thicknesses (see Fig. 11).

APPENDIX B: RELATION BETWEEN GROOVE DIMENSIONS AND TIME

In bulk diffusion-driven grain-boundary grooving, the groove dimensions (i.e., the combined groove depth $d_g + d_h$) double in size whenever the time increases by a factor of eight. We know that the relationship between the groove depth and time is given by the equation

$$d_g(t) + d_h(t) = k \cdot t^{1/3}.$$

Now, let us express the combined groove depth $d'_g + d'_h$ for a time $t' = 8t$, such that

$$d'_g(t') + d'_h(t') = k \cdot (8t)^{1/3} = k \cdot 8^{1/3} \cdot t^{1/3},$$

$$d'_g(t') + d'_h(t') = 2 \cdot k \cdot t^{1/3}.$$

Comparing this with the original equation, we see that

$$d'_g(t') + d'_h(t') = 2 \cdot (d_g(t) + d_h(t)).$$

Henceforth, when time increases by a factor of eight, groove depth $d_g + d_h$ doubles.

REFERENCES

¹R. L. Coble, "Sintering crystalline solids. II. Experimental test of diffusion models in powder compacts," *J. Appl. Phys.* **32**, 793–799 (1961).

- ²T. Gladman, "On the theory of the effect of precipitate particles on grain growth in metals," *Proc. R. Soc. Lond. Ser. A* **294**, 298–309 (1966).
- ³P. Barna and M. Adamik, "Fundamental structure forming phenomena of polycrystalline films and the structure zone models," *Thin Solid Films* **317**, 27–33 (1998).
- ⁴D. Jones, "The measurement of solid-liquid interfacial energies from the shapes of grain-boundary grooves," *Philos. Mag.* **27**, 569–584 (1973).
- ⁵W. W. Mullins, "Theory of thermal grooving," *J. Appl. Phys.* **28**, 333–339 (1957).
- ⁶W. Mullins, "Grain boundary grooving by volume diffusion," *Trans. Am. Inst. Min. Metall. Eng.* **218**, 354–361 (1960).
- ⁷J. Schölhammer, B. Baretzky, W. Gust, E. Mittemeijer, and B. Straumal, "Grain boundary grooving as an indicator of grain boundary phase transformations," *Interface Sci.* **9**, 43–53 (2001).
- ⁸M. McLean and E. Hondros, "A study of grain-boundary grooving at the platinum/alumina interface," *J. Mater. Sci.* **6**, 19–24 (1971).
- ⁹L. Klinger and E. Rabkin, "Effects of surface anisotropy on grain boundary grooving," *Interface Sci.* **9**, 55–63 (2001).
- ¹⁰F. Genin, W. Mullins, and P. Wynblatt, "The effect of stress on grain boundary grooving," *Acta Metall. Mater.* **41**, 3541–3547 (1993).
- ¹¹R. Trivedi and W. Kurz, "Dendritic growth," *Int. Mater. Rev.* **39**, 49–74 (1994).
- ¹²G. Bolling and W. Tiller, "Growth from the melt. I. Influence of surface inter-sections in pure metals," *J. Appl. Phys.* **31**, 1345–1350 (1960).
- ¹³G. Nash and M. Glicksman, "A general method for determining solid-liquid interfacial free energies," *Philos. Mag.* **24**, 577–592 (1971).
- ¹⁴W. Zhang and I. Gladwell, "Thermal grain boundary grooving with anisotropic surface free energy in three dimensions," *J. Cryst. Growth* **277**, 608–622 (2005).
- ¹⁵D. Min and H. Wong, "Grain-boundary grooving by surface diffusion with asymmetric and strongly anisotropic surface energies," *J. Appl. Phys.* **99**, 023515 (2006).
- ¹⁶V. P. Laxmipathy, F. Wang, M. Selzer, and B. Nestler, "A two-dimensional phase-field study on dendritic growth competition under convective conditions," *Comput. Mater. Sci.* **186**, 109964 (2021).
- ¹⁷V. P. Laxmipathy, F. Wang, M. Selzer, and B. Nestler, "Phase-field simulations of grain boundary grooving under diffusive-convective conditions," *Acta Mater.* **204**, 116497 (2021).
- ¹⁸V. P. Laxmipathy, F. Wang, M. Selzer, B. Nestler, and K. Ankit, "Influence of melt convection on the morphological evolution of seaweed structures: Insights from phase-field simulations," *Comput. Mater. Sci.* **170**, 109196 (2019).
- ¹⁹J.-H. Jeong, N. Goldenfeld, and J. A. Dantzig, "Phase field model for three-dimensional dendritic growth with fluid flow," *Phys. Rev. E* **64**, 041602 (2001).
- ²⁰N. Moelans, B. Blanpain, and P. Wollants, "A phase field model for grain growth and thermal grooving in thin films with orientation dependent surface energy," *Solid State Phenom.* **129**, 89–94 (2007).
- ²¹S. Yeh, C. Chen, and C. Lan, "Phase field modeling of morphological instability near grain boundary during directional solidification of a binary alloy: The hump formation," *J. Cryst. Growth* **324**, 296–303 (2011).
- ²²M. Verma and R. Mukherjee, "Effect of surface energy anisotropy on hole growth in a single-crystalline thin film: A phase-field study," *Scr. Mater.* **234**, 115572 (2023).
- ²³A. Mukherjee, K. Ankit, M. Selzer, and B. Nestler, "Electromigration-induced surface drift and slit propagation in polycrystalline interconnects: Insights from phase-field simulations," *Phys. Rev. Appl.* **9**, 044004 (2018).
- ²⁴A. Mukherjee, K. Ankit, M. Selzer, and B. Nestler, "Phase-field modelling of electromigration-induced intergranular slit propagation in metal interconnects," *Comput. Mater. Sci.* **228**, 112330 (2023).
- ²⁵P. W. Hoffrogge, A. Mukherjee, E. Nani, P. K. Amos, F. Wang, D. Schneider, and B. Nestler, "Multiphase-field model for surface diffusion and attachment kinetics in the grand-potential framework," *Phys. Rev. E* **103**, 033307 (2021).
- ²⁶A. Choudhury and B. Nestler, "Grand-potential formulation for multicomponent phase transformations combined with thin-interface asymptotics of the double-obstacle potential," *Phys. Rev. E* **85**, 021602 (2012).

10 April 2025 10:34:40

- ²⁷P. L. Veluvali, "Phase-field modeling of unidirectionally solidified microstructures under diffusive-convective regime," Ph.D. thesis dissertation [Karlsruher Institut für Technologie (KIT), Karlsruhe, 2021].
- ²⁸V. P. Laxmipathy, F. Wang, M. Selzer, and B. Nestler, "A two-dimensional phase-field investigation on unidirectionally solidified tip-splitting microstructures," *Metals* **12**, 376 (2022).
- ²⁹V. P. Laxmipathy, F. Wang, M. Selzer, and B. Nestler, "Microstructural transition in monotectic alloys: A phase-field study," *Int. J. Heat Mass Transfer* **159**, 120096 (2020).
- ³⁰B. Nestler, H. Garcke, and B. Stinner, "Multicomponent alloy solidification: Phase-field modeling and simulations," *Phys. Rev. E* **71**, 041609 (2005).
- ³¹B. Bokstein, L. M. Klinger, and I. Apikhtina, "Liquid grooving at grain boundaries," *Mater. Sci. Eng. A* **203**, 373–376 (1995).
- ³²C. Herring, "Some theorems on the free energies of crystal surfaces," *Phys. Rev.* **82**, 87 (1951).
- ³³O. Tschukin, A. Silberzahn, M. Selzer, P. G. Amos, D. Schneider, and B. Nestler, "Concepts of modeling surface energy anisotropy in phase-field approaches," *Geotherm. Energy* **5**, 1–21 (2017).
- ³⁴W. Zhang, P. Sachenko, and I. Gladwell, "Thermal grain boundary grooving with anisotropic surface free energies," *Acta Mater.* **52**, 107–116 (2004).
- ³⁵O. Akyildiz, E. E. Oren, and T. O. Ogurtani, "Grain boundary grooving in bi-crystal thin films induced by surface drift-diffusion driven by capillary forces and applied uniaxial tensile stresses," *Philos. Mag.* **92**, 804–829 (2012).
- ³⁶T. Xin and H. Wong, "Grain-boundary grooving by surface diffusion with strong surface energy anisotropy," *Acta Mater.* **51**, 2305–2317 (2003).
- ³⁷A. Ramasubramaniam and V. Shenoy, "On the evolution of faceted grain-boundary grooves by surface diffusion," *Acta Mater.* **53**, 2943–2956 (2005).
- ³⁸T. Takaki, M. Ohno, T. Shimokawabe, and T. Aoki, "Two-dimensional phase-field simulations of dendrite competitive growth during the directional solidification of a binary alloy bicrystal," *Acta Mater.* **81**, 272–283 (2014).
- ³⁹P. Voorhees, S. Coriell, G. McFadden, and R. Sekerka, "The effect of anisotropic crystal-melt surface tension on grain boundary groove morphology," *J. Cryst. Growth* **67**, 425–440 (1984).
- ⁴⁰B. Caroli, C. Caroli, G. Faivre, and J. Mergy, "Lamellar eutectic growth of $\text{CBr}_4\text{-C}_2\text{Cl}_6$: Effect of crystal anisotropy on lamellar orientations and wavelength dispersion," *J. Cryst. Growth* **118**, 135–150 (1992).